Progress In Electromagnetics Research C, Vol. 132, 255–269, 2023

Load Angle of Flux Modulated Magnetic Gears

Rong-Jie Wang[1, *], Stanley Robert Holm[2], Josh Scheepers[1], and Stiaan Gerber[1]

Abstract—In this paper, the authors address the issue of flux-modulated magnetic gear (FMMG), which offers many potential advantages over traditional mechanical gears for a wide range of applications. In the proposed FMMG model, two permanent magnet (PM) carriers are of different pole-pairs and rotate asynchronously, and their relative angular position with respect to the pole parts of the flux modulator is not as straightforward and simple as it may seem in conventional electrical machines. Therefore, this paper focuses on the details of the derivation of FMMG load angle, which attempts to better express the angular relationship between the individual components of an FMMG. Finite element method (FEM) simulations and experiments are used to validate the load angle concept and corresponding results, and are complemented by experimental measurements. It is believed that the concept of loading angle can facilitate the design and simulation of FMMG and magnetically geared machines (MGM) based on the finite element method under different loading conditions.

1. INTRODUCTION

In the past two decades, magnetic gear (MG) technologies are receiving considerable attention worldwide, which is evident from the histogram of the number of related publications [1–5] (including *research papers, theses, patents, and research reports*) shown in Figure 1. Among the promising MG topologies, such as harmonic [6], planetary [7, 8], and flux modulated MGs [9], flux modulated

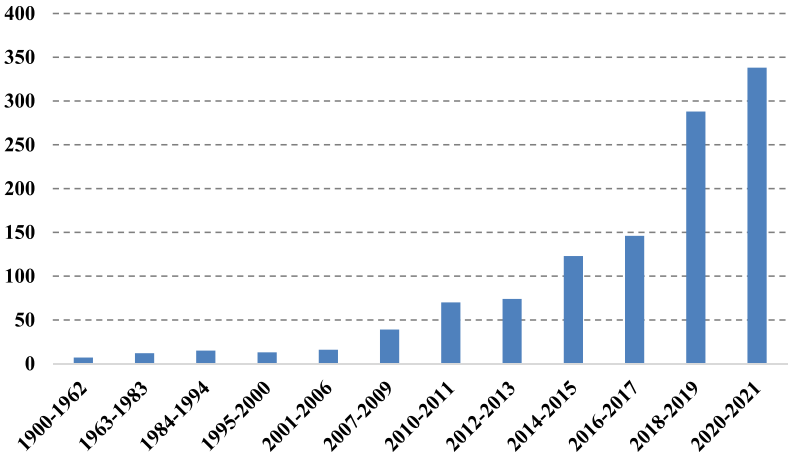

Figure 1. The published work on magnetic gear technologies (1900–2021).

Received 16 March 2023, Accepted 29 April 2023, Scheduled 7 May 2023
* Corresponding author: Rong-Jie Wang (rwang@sun.ac.za).
[1] Department of Electrical & Electronic Engineering, Stellenbosch University, Matieland 7602, South Africa. [2] CSIR, Meiring Naude Rd, Brummeria, Pretoria, South Africa.

magnetic gear (FMMG) has received the most attention and has been the focus of research and development. This is largely due to its relatively simple mechanical construction and the concentric structure that makes provision for a compact machine-gear integration option. A typical FMMG consists of three concentric components, i.e., a high pole-count permanent magnet (PM) carrier, a low pole-count PM carrier, and a flux modulator between them. The gearing function is performed by fixing one of the concentric components (usually the flux modulator) and allowing the other two components to act as input/output mechanical ports. In this configuration, the low pole-count and high pole-count PM carriers are often referred as high-speed (HS) rotor and low-speed (LS) rotor, respectively. Although radial flux FMMG is the most common [10–15], based on the same working principle, the FMMG can also be designed for axial flux topology [16, 17] as shown in Figure 2.

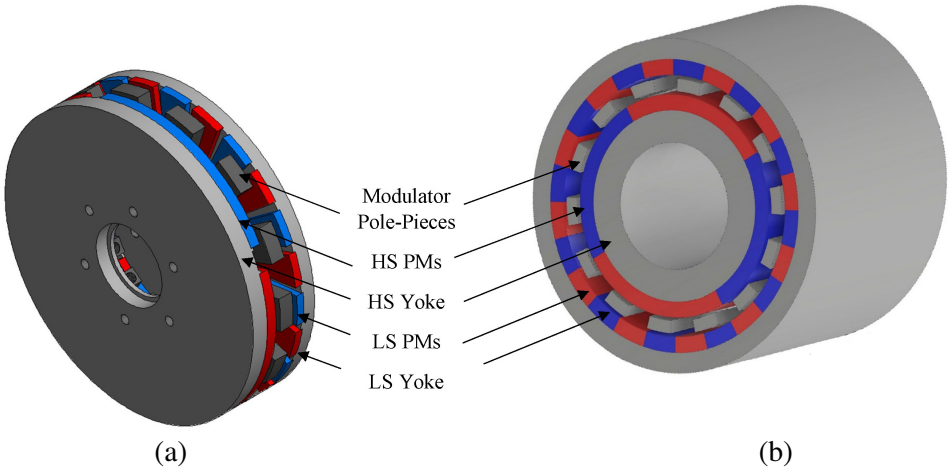

Figure 2. Coaxial flux modulated MG topologies; (a) axial flux type, (b) radial flux type.

Since the two PM carriers have different pole-pairs and rotate asynchronously, their relative angular positions with regard to the pole-pieces of the flux modulator are not as simple and intuitive as for classical electrical machines [18]. For the design of magnetic gears, finite element method (FEM) is undoubtedly the most commonly used. The normal practice is to set up these rotor positions to realize a maximum transmission torque (also called *stall torque*) of the FMMG [19]. Surprisingly, no basic theory can be found in literature that provides basic guidance on how to choose these initial angles. Researchers seem to be contented with their empirical ways or methods to determine these initial angles [20]. An interesting concept of load angle was introduced in [21], in which the relationship between the transmissible torque and angular positions of FMMG's concentric components was first revealed. However, because of the scope of the paper, the mathematical derivation was treated in a brief and simplified manner without necessary validation. As a result, the significance of the load angle of FMMGs has not been well recognized.

This paper presents a detailed derivation of the load angle of FMMGs, which are validated by both finite element (FE) simulation and experimental measurements. Further, it attempts to provide a better understanding of the angular relationship between the concentric components of an FMMG, which can facilitate the FEM based design and simulation of FMMGs under different load conditions. The remaining part of the paper is organized as follows. In Section 2, the derivation of load angle for FMMGs is presented. The experimental validation on a physical FMMG is described in Section 3. Then, the application of the load angle concept in the design of FMMGs is discussed in Section 4, and thereafter, conclusions are drawn.

2. DERIVATION OF THE LOAD ANGLE OF FMMGS

In this study, the analytical derivation will be conducted for an axial flux FMMG. This is mainly due to its unique disc-type mechanical layout, which provides easy access to each co-axial FMMG component

for experimental investigations. However, the derived load angle concept and angular relationship of an axial flux FMMG is just as applicable to other FMMG topologies.

Figure 3 demonstrates the reference angles of a singular PM on each rotor disc and a modulator segment. θ_L and θ_H align with the centre of a PM of their respective rotor and are measured relative to a common reference angle. θ_M aligns with the centre of a modulator segment, and it is also measured relative to the same common reference angle.

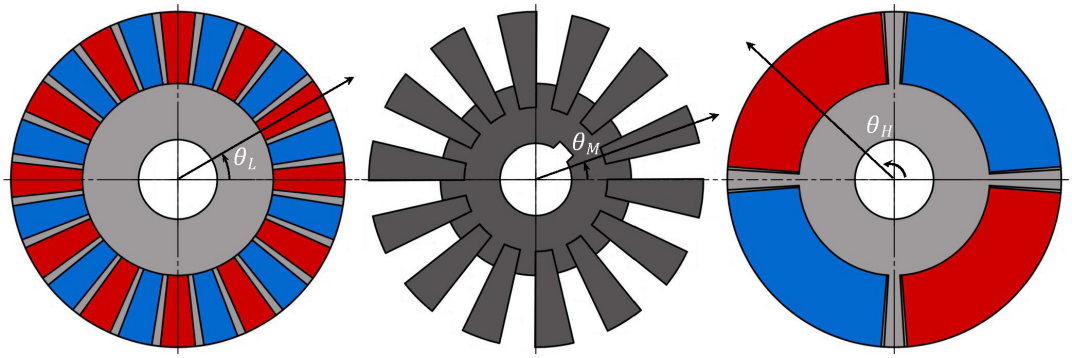

Figure 3. Component angular relationship.

2.1. Principle of Operation

The following Fourier series expressions shown in (1) and (2) describe the magneto-motive force (MMF) patterns created by the alternating axial magnetizations of the PMs on both HS and LS rotors. These MMF patterns created by the PMs pole-pairs result in half wave symmetry of the output, and the summation is reduced to odd harmonics. Equation (3) accounts for the permeance function of the axial-flux path between the air-gaps of each rotor [17].

$$\mathcal{F}_H = \sum_{i=1,3,5,\ldots}^{\infty} M_{Hi}(r,z) \cdot \cos\left[i \cdot p_H \left(\theta - \omega_H \cdot t - \theta_H\right)\right] \tag{1}$$

$$\mathcal{F}_L = \sum_{j=1,3,5,\ldots}^{\infty} M_{Lj}(r,z) \cdot \cos\left[j \cdot p_L \left(\theta - \omega_L \cdot t - \theta_L\right)\right] \tag{2}$$

$$\mathcal{P} = \mathcal{P}_{avg}(r,z) + \sum_{k=1,2,3,\ldots}^{\infty} \mathcal{P}_{Modk}(r,z) \cdot \cos\left[k \cdot q_M \left(\theta - \omega_M \cdot t - \theta_M\right)\right] \tag{3}$$

where $M_{Hi}(r,z)$ and $M_{Lj}(r,z)$ are the MMF harmonic magnitudes, which are assumed to be constant and distributed evenly over the surface of the magnets for simplification of the model. They are subsequently referred to as M_{Hi} and M_{Lj}. $\mathcal{P}_{avg}(r,z)$ accounts for the combined reluctance of the yokes, air-gaps and magnets, while $\mathcal{P}_{Modk}(r,z)$ represents the difference in reluctance due to the position of the modulator segments.

Using (1) and (3), the flux in the LS side air-gap due to the PMs on HS rotor is:

$$\begin{aligned}\phi_{Hm} = &\left\{\sum_{i=1,3,5,\ldots}^{\infty} M_{Hi} \cdot \cos\left[i \cdot p_H \left(\theta - \omega_H \cdot t - \theta_H\right)\right]\right\} \\ &\cdot \left\{\mathcal{P}_{avg} + \sum_{k=1,2,3,\ldots}^{\infty} \mathcal{P}_{Modk} \cdot \cos\left[k \cdot q_M \left(\theta - \omega_M \cdot t - \theta_M\right)\right]\right\}\end{aligned} \tag{4}$$

Likewise, the modulated flux in the HS side air-gap due to the PMs on LS rotor is:

$$\phi_{Lm} = \left\{ \sum_{j=1,3,5,\ldots}^{\infty} M_{Lj} \cdot \cos\left[j \cdot p_L \left(\theta - \omega_L \cdot t - \theta_L\right)\right] \right\} \cdot \left\{ \mathcal{P}_{avg} + \sum_{k=1,2,3,\ldots}^{\infty} \mathcal{P}_{Modk} \cdot \cos\left[k \cdot q_M \left(\theta - \omega_M \cdot t - \theta_M\right)\right] \right\} \quad (5)$$

Using identity $\cos A \cos B = \frac{1}{2}[\cos(A+B) + \cos(A-B)]$, the above equations can be expanded as follows:

$$\begin{aligned}\phi_{Hm} = {} & \mathcal{P}_{avg} \cdot \left\{ \sum_{i=1,3,5,\ldots}^{\infty} M_{Hi} \cdot \cos\left[i \cdot p_H \left(\theta - \omega_H \cdot t - \theta_H\right)\right] \right\} + \frac{1}{2} \sum_{i=1,3,5,\ldots}^{\infty} \sum_{k=1,2,3,\ldots}^{\infty} M_{Hi} \cdot \mathcal{P}_{Modk} \\ & \cdot \cos\left\{ \left(i \cdot p_H + k \cdot q_M\right) \left[\theta - \frac{i \cdot p_H \cdot \omega_H + k \cdot q_M \cdot \omega_M}{i \cdot p_H + k \cdot q_M} \cdot t \right.\right. \\ & \left.\left. - \left(i \cdot p_H \cdot \theta_H + k \cdot q_M \theta_M\right) \right] \right\} + \frac{1}{2} \sum_{i=1,3,5,\ldots}^{\infty} \sum_{k=1,2,3,\ldots}^{\infty} M_{Hi} \cdot \mathcal{P}_{Modk} \\ & \cdot \cos\left\{ \left(i \cdot p_H - k \cdot q_M\right) \left[\theta - \frac{i \cdot p_H \cdot \omega_H - k \cdot q_M \cdot \omega_M}{i \cdot p_H - k \cdot q_M} \cdot t - \left(i \cdot p_H \cdot \theta_H - k \cdot q_M \theta_M\right) \right] \right\} \end{aligned} \quad (6)$$

$$\begin{aligned}\phi_{Lm} = {} & \mathcal{P}_{avg} \cdot \left\{ \sum_{j=1,3,5,\ldots}^{\infty} M_{Lj} \cdot \cos\left[j \cdot p_L \left(\theta - \omega_L \cdot t - \theta_L\right)\right] \right\} + \frac{1}{2} \sum_{j=1,3,5,\ldots}^{\infty} \sum_{k=1,2,3,\ldots}^{\infty} M_{Lj} \cdot \mathcal{P}_{Modk} \\ & \cdot \cos\left\{ \left(j \cdot p_L + k \cdot q_M\right) \left[\theta - \frac{j \cdot p_L \cdot \omega_L + k \cdot q_M \cdot \omega_M}{j \cdot p_L + k \cdot q_M} \cdot t \right.\right. \\ & \left.\left. - \left(j \cdot p_L \cdot \theta_L + k \cdot q_M \theta_M\right) \right] \right\} + \frac{1}{2} \sum_{j=1,3,5,\ldots}^{\infty} \sum_{k=1,2,3,\ldots}^{\infty} M_{Lj} \cdot \mathcal{P}_{Modk} \\ & \cdot \cos\left\{ \left(j \cdot p_L - k \cdot q_M\right) \left[\theta - \frac{j \cdot p_L \cdot \omega_L - k \cdot q_M \cdot \omega_M}{j \cdot p_L - k \cdot q_M} \cdot t - \left(j \cdot p_L \cdot \theta_L - k \cdot q_M \theta_M\right) \right] \right\} \end{aligned} \quad (7)$$

By analysing these equations, the theoretical air-gap flux spatial harmonic components can be determined. This is shown in (8) and (9) and represents the effective pole pair and modulator segment relationship. Equations (10) and (11) describe the relationship between the components' angular velocities:

$$p_{i,k} = |i \cdot p_H + k \cdot q_M| \quad (8)$$

$$p_{j,k} = |j \cdot p_L + k \cdot q_M| \quad (9)$$

$$\omega_{i,k} = \frac{i \cdot p_H \cdot \omega_H + k \cdot q_M \cdot \omega_M}{i \cdot p_H + k \cdot q_M} \quad (10)$$

$$\omega_{j,k} = \frac{j \cdot p_L \cdot \omega_L + k \cdot q_M \cdot \omega_M}{j \cdot p_L + k \cdot q_M} \quad (11)$$

$$i = 1, 3, 5... \quad j = 1, 3, 5... \quad k = 0, \pm 1, \pm 2...$$

For an effective gearing action between the rotors, a coupling is required of the fundamental component of flux created by either set of PMs with a component of the modulated flux of the other rotor. As explained in [9, 17], the highest asynchronous spacial harmonic is produced when i or $j = 1$ and $k = -1$, and therefore, the relationship of pole-pairs to modulator segments can be described as:

$$p_L = |p_H - q_M| \quad \text{with} \quad (p_H < p_L) \quad (12)$$

With the condition satisfied this yields two possible solutions, of which $q_M = p_H + p_L$ in practice provides the most effective solution. When the modulator is held stationary, ω_M is zero, and the formula for the angular velocity relationship is reduced to

$$\omega_L = \frac{p_H \cdot \omega_H}{p_H - q_M}$$

From this result, the gear ratio for the stationary modulator can be described as

$$G_M = \frac{\omega_L}{\omega_H} = \frac{p_H}{-p_L} \tag{13}$$

In general, the respective velocity relationship of the components can be described as

$$p_L \cdot \omega_L + p_H \cdot \omega_H = q_M \cdot \omega_M \tag{14}$$

By considering only the highest asynchronous space harmonic, (i.e., $i, j = 1$; $k = -1$), Equations (4) and (5) are reduced to:

$$\phi_{Hm} = \{M_H \cdot \cos[p_H(\theta - \omega_H \cdot t - \theta_H)]\} \cdot \{\mathcal{P}_{avg} + \mathcal{P}_{Mod} \cdot \cos[-q_M(\theta - \omega_M \cdot t - \theta_M)]\} \tag{15}$$

$$\phi_{Lm} = \{M_L \cdot \cos[p_L(\theta - \omega_L \cdot t - \theta_L)]\} \cdot \{\mathcal{P}_{avg} + \mathcal{P}_{Mod} \cdot \cos[-q_M(\theta - \omega_M \cdot t - \theta_M)]\} \tag{16}$$

Evaluating (15) and (16) at time $t = 0$, the modulated flux in the LS and HS air-gaps is further simplified as:

$$\phi_{Hm} = M_H \cdot \mathcal{P}_{avg} \cdot \cos[p_H(\theta - \theta_H)] + M_H \cdot \mathcal{P}_{Mod} \cdot \cos[p_H(\theta - \theta_H)] \cos[-q_M(\theta - \theta_M)] \tag{17}$$

$$\phi_{Lm} = M_L \cdot \mathcal{P}_{avg} \cdot \cos[p_L(\theta - \theta_L)] + M_L \cdot \mathcal{P}_{Mod} \cdot \cos[p_L(\theta - \theta_L)] \cos[-q_M(\theta - \theta_M)] \tag{18}$$

Again, they are expanded as follows:

$$\begin{aligned}\phi_{Hm} = {} & M_H \cdot \mathcal{P}_{avg} \cdot \cos[p_H(\theta - \theta_H)] + \frac{1}{2} M_H \cdot \mathcal{P}_{Mod} \cdot \cos[p_H(\theta - \theta_H) - q_M(\theta - \theta_M)] \\ & + \frac{1}{2} M_H \cdot \mathcal{P}_{Mod} \cdot \cos[p_H(\theta - \theta_H) + q_M(\theta - \theta_M)]\end{aligned} \tag{19}$$

$$\begin{aligned}\phi_{Lm} = {} & M_L \cdot \mathcal{P}_{avg} \cdot \cos[p_L(\theta - \theta_L)] + \frac{1}{2} M_L \cdot \mathcal{P}_{Mod} \cdot \cos[p_L(\theta - \theta_L) - q_M(\theta - \theta_M)] \\ & + \frac{1}{2} M_L \cdot \mathcal{P}_{Mod} \cdot \cos[p_L(\theta - \theta_L) + q_M(\theta - \theta_M)]\end{aligned} \tag{20}$$

Since the magnetic flux in the adjacent air-gap of MMF source can be expressed as:

$$\phi_H = M_H \cdot \mathcal{P}_{avg} \cdot \cos[p_H(\theta - \theta_H)] \tag{21}$$

$$\phi_L = M_L \cdot \mathcal{P}_{avg} \cdot \cos[p_L(\theta - \theta_L)] \tag{22}$$

The total flux in each air-gap is the summation ϕ_x and ϕ_{xm} resulting in

$$\phi_{TH} = \phi_H + \phi_{Lm} \tag{23}$$

$$\phi_{TL} = \phi_L + \phi_{Hm} \tag{24}$$

It should be noted that the following assumption has been made to simplify the analysis [21]:

$$\int_0^{2\pi} |\phi_x| d\theta = \int_0^{2\pi} |\phi_{xm}| d\theta \tag{25}$$

which implies that there is a continuity of magnetic flux in the integration region (no leakage flux).

2.2. Torque Calculation

The calculation of torque on the rotors now follows the approach described in [22]. The flux density in the regions of the FMMG is defined as:

$$B(r, \theta) = \frac{\phi_{Tx}}{A_x} \tag{26}$$

The general co-energy equation in the air-gaps is defined as

$$W' = \frac{1}{2 \cdot \mu_o} \int_V B^2 \, dv \tag{27}$$

For this axial-flux model it can be further calculated as

$$W' = \frac{1}{2 \cdot \mu_o} \int_0^{2\pi} \int_0^Z \int_{r_i}^{r_o} \frac{\phi_{Tx}^2(\theta)}{(\pi \cdot r^2)^2} \, r dr dz d\theta \tag{28}$$

$$W' = \underbrace{\frac{Z_x}{-4 \cdot \mu_o \cdot \pi^2 (r_o^2 - r_i^2)}}_{C_x} \int_0^{2\pi} \phi_{Tx}^2(\theta) d\theta \tag{29}$$

where Z_x is the axial distance between rotor disc and the modulator for each region (Z_H and Z_L for the high-speed and low-speed regions, respectively).

The remaining integral of the co-energy equation is calculated for each region as

$$\begin{aligned} I_{\phi_{TH}} &= \int_0^{2\pi} \phi_{TH}^2(\theta) d\theta \\ &= \Big\{ M_H \cdot \mathcal{P}_{avg} \cdot \cos\left[p_H \left(\theta - \theta_H\right)\right] + M_L \cdot \mathcal{P}_{avg} \cdot \cos\left[p_L \left(\theta - \theta_L\right)\right] \\ &\quad + \frac{1}{2} M_L \cdot \mathcal{P}_{Mod} \cdot \cos\left[p_L \left(\theta - \theta_L\right) - q_M \left(\theta - \theta_M\right)\right] \\ &\quad + \frac{1}{2} M_L \cdot \mathcal{P}_{Mod} \cdot \cos\left[p_L \left(\theta - \theta_L\right) + q_M \left(\theta - \theta_M\right)\right] \Big\}^2 \end{aligned} \tag{30}$$

$$\begin{aligned} I_{\phi_{TL}} &= \int_0^{2\pi} \phi_{TL}^2(\theta) d\theta \\ &= \Big\{ M_L \cdot \mathcal{P}_{avg} \cdot \cos\left[p_L \left(\theta - \theta_L\right)\right] + M_H \cdot \mathcal{P}_{avg} \cdot \cos\left[p_H \left(\theta - \theta_H\right)\right] \\ &\quad + \frac{1}{2} M_H \cdot \mathcal{P}_{Mod} \cdot \cos\left[p_H \left(\theta - \theta_H\right) - q_M \left(\theta - \theta_M\right)\right] \\ &\quad + \frac{1}{2} M_H \cdot \mathcal{P}_{Mod} \cdot \cos\left[p_H \left(\theta - \theta_H\right) + q_M \left(\theta - \theta_M\right)\right] \Big\}^2 \end{aligned} \tag{31}$$

The expansion of Equations (30) and (31) yields terms that can be expressed in the form of either (A1) or (A8). Using (A7) and (A8) to evaluate the integrals, the following simplified equations can be obtained:

$$\begin{aligned} I_{\phi_{TH}} &= M_H \cdot M_L \cdot \mathcal{P}_{avg} \cdot \mathcal{P}_{Mod} \cdot \cos\left(q_M \theta_M - p_L \theta_L - p_H \theta_H\right) \\ &\quad + \frac{\pi \cdot M_L^2 \cdot \mathcal{P}_{Mod}^2}{2} + \pi \cdot M_L^2 \cdot \mathcal{P}_{avg}^2 + \pi \cdot M_H^2 \cdot \mathcal{P}_{avg}^2 \end{aligned} \tag{32}$$

$$\begin{aligned} I_{\phi_{TL}} &= M_H \cdot M_L \cdot \mathcal{P}_{avg} \cdot \mathcal{P}_{Mod} \cdot \cos\left(q_M \theta_M - p_L \theta_L - p_H \theta_H\right) \\ &\quad + \frac{\pi \cdot M_H^2 \cdot \mathcal{P}_{Mod}^2}{2} + \pi \cdot M_L^2 \cdot \mathcal{P}_{avg}^2 + \pi \cdot M_H^2 \cdot \mathcal{P}_{avg}^2 \end{aligned} \tag{33}$$

The electromagnetic torque induced on a component of an FMMG is defined as the change in co-energy in both regions due to the relative angular position of the specified component. The resulting torque on the modulator is the summation of the torque of the two rotors.

$$T_H = \frac{\partial W_H'}{\partial \theta_H} + \frac{\partial W_L'}{\partial \theta_H} = \frac{\partial (C_H I_{\phi_{TH}})}{\partial \theta_H} + \frac{\partial (C_L I_{\phi_{TL}})}{\partial \theta_H} \tag{34}$$

$$T_L = \frac{\partial W_H'}{\partial \theta_L} + \frac{\partial W_L'}{\partial \theta_L} = \frac{\partial (C_H I_{\phi_{TH}})}{\partial \theta_L} + \frac{\partial (C_L I_{\phi_{TL}})}{\partial \theta_L} \tag{35}$$

$$T_{Mod} = T_H + T_L \tag{36}$$

By substituting in the constants and simplifying, the torque on each component can be calculated as follows:

$$\begin{aligned} T_H &= \frac{p_H \cdot (Z_H + Z_L) \cdot M_H \cdot M_L \cdot \mathcal{P}_{avg} \cdot \mathcal{P}_{Mod}}{4 \cdot \mu_o \cdot \pi^2 (r_o^2 - r_i^2)} \cdot \sin\left(p_L\theta_L + p_H\theta_H - q_M\theta_M\right) \\ T_L &= \frac{p_L \cdot (Z_H + Z_L) \cdot M_H \cdot M_L \cdot \mathcal{P}_{avg} \cdot \mathcal{P}_{Mod}}{4 \cdot \mu_o \cdot \pi^2 (r_o^2 - r_i^2)} \cdot \sin\left(p_L\theta_L + p_H\theta_H - q_M\theta_M\right) \\ T_{Mod} &= \frac{q_M \cdot (Z_H + Z_L) \cdot M_H \cdot M_L \cdot \mathcal{P}_{avg} \cdot \mathcal{P}_{Mod}}{4 \cdot \mu_o \cdot \pi^2 (r_o^2 - r_i^2)} \cdot \sin\left(p_L\theta_L + p_H\theta_H - q_M\theta_M\right) \end{aligned} \tag{37}$$

2.3. Definition of the Load Angle

From these equations, the implicit derivation of the load angle is observed as

$$\delta_g = p_L\theta_L + p_H\theta_H - q_M\theta_M \tag{38}$$

This load angle describes the relationship between the torque output of an FMMG and the angular positions of the rotors and modulator. From the above equations, some interesting observations can be made, i.e.,

- Based on simple laws of trigonometry, an FMMG achieves the maximum torque when the load angle $\delta_g = 90^\circ$ while it realizes the minimum (zero) torque when $\delta_g = 0^\circ$;
- For a given load condition (thus a constant δ_g) of FMMG, the general angular velocity relationship among FMMG components, i.e., Equation (14), can be obtained by differentiating (38) with regard to time;
- Since $p_L + p_H = q_M$ for an FMMG, δ_g determined at another circumferential position with a $\Delta\theta$ displacement can be expressed as follows:

$$p_L(\theta_L + \Delta\theta) + p_H(\theta_H + \Delta\theta) - q_M(\theta_M + \Delta\theta) = p_L\theta_L + p_H\theta_H - q_M\theta_M$$

Thus, a load angle calculated from any FMMG angular position is essentially the same.

3. TORQUE-LOAD ANGLE CHARACTERISTICS

Based on the load angle concept, the torque characteristics of a magnet gear simply becomes a function of load angle irrespective of number of PM poles and physical angles. This essentially makes it more convenient to model and compare different FMMGs under specific load conditions. Although the load angle is a function of three offset angles of FMMG components with regard to an arbitrary reference, a simple way of obtaining the torque-load angle characteristics of an FMMG component is to vary its offset angle while keeping the other two offset angles at zero. Figure 4 shows the torque-load angle characteristics of a prototype axial flux FMMG obtained by using (37). A photo of the axial flux FMMG prototype is displayed in Figure 5, and its design specifications are summarized in Table 1.

Alternatively, finite element method can also be used to produce these torque-load angle characteristics. Figure 6 shows the three offset angles and their transition into a simple 2D FE model of an axial flux FMMG. In this case, three offset angles θ_L, θ_M, and θ_H are all aligned with a reference line, which means $\delta_g = 0$ (no-load condition). Figure 7 shows the flux distribution of the axial flux FMMG at a time step, where the load angle is 0°. The software package used for the simulation is Ansys Electronics Desktop.

To realize a 90° degree load angle for an FMMG, either the HS rotor or the LS rotor should be rotated by $90^\circ/p_H$ or $90^\circ/p_L$, respectively. Figure 8 shows 2D FE model of an axial flux FMMG where either LS rotor or HS rotor shifts half a pole-pitch resulting in a load angle of 90°. The 2D FE simulated torque-load angle characteristics of the prototype FMMG are illustrated in Figure 9, which shows a good agreement with the analytically calculated results.

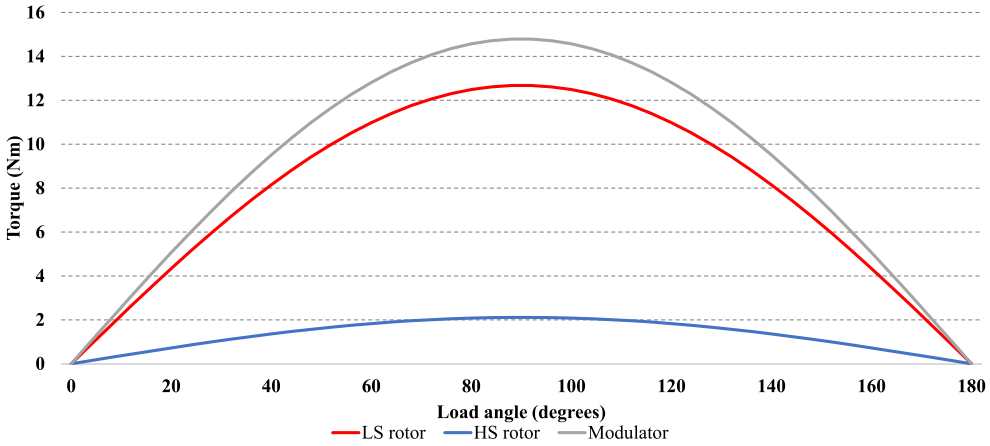

Figure 4. Analytically calculated torque-load angle curves of an axial flux FMMG.

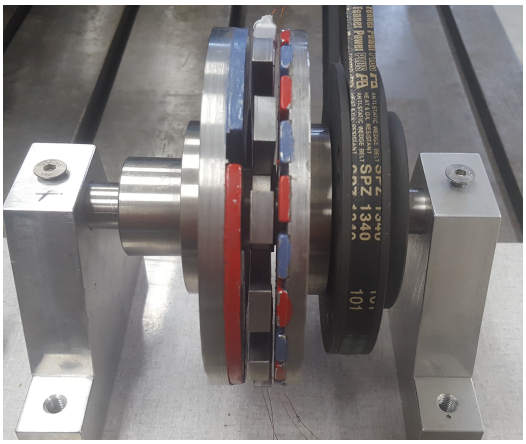

Figure 5. A photo of the axial flux FMMG prototype used in the study.

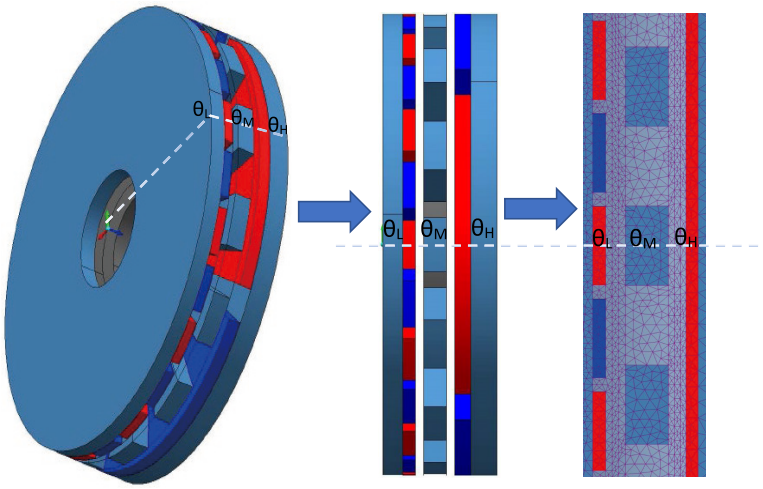

Figure 6. 2-D FE model of the axial flux FMMG prototype.

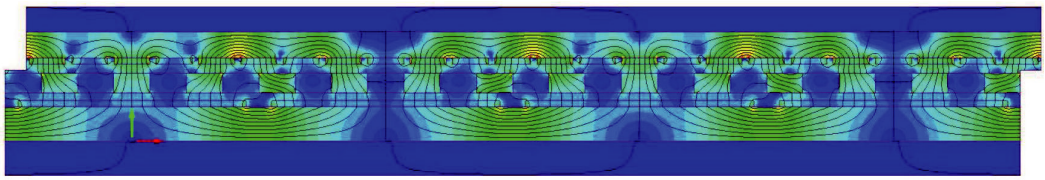

Figure 7. Flux distribution in the 2D FE model of an axial flux FMMG at a time step where $\delta_g = 0°$.

Table 1. Design specifications of the axial flux FMMG prototype.

Components	Specifications
HS rotor pole-pairs	2
LS rotor pole-pairs	12
Modulator pole-pieces	14
PM outer radius (mm)	70
PM inner radius (mm)	40
HS rotor yoke thickness (mm)	8
HS rotor PM thickness (mm)	4.8
HS rotor PM pitch angle	81°
HS rotor side air-gap length (mm)	2.5
LS rotor yoke thickness (mm)	6
LS rotor PM thickness (mm)	3.7
LS rotor PM pitch angle	12°
LS rotor side air-gap length (mm)	2.5
Modulator pole-piece thickness (mm)	7
Modulator pole-piece pitch angle	13.4°

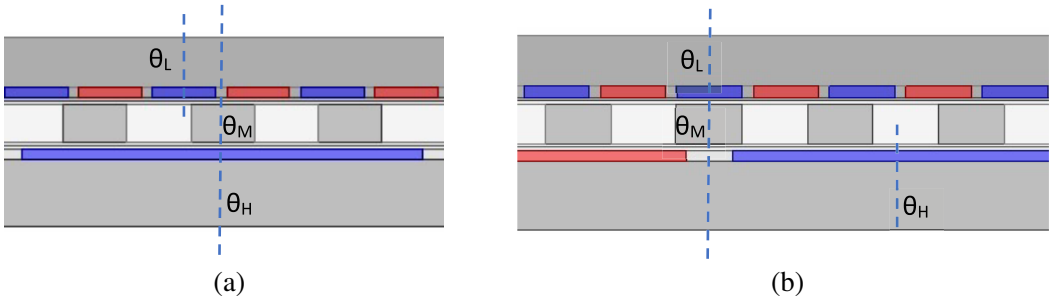

Figure 8. 2D FE model of an axial flux FMMG with $\delta_g = 90°$ by offsetting (a) the LS rotor or (b) HS rotor with a half pole-pitch.

4. EXPERIMENTAL INVESTIGATION

The torque-load angle characteristics of the axial flux FMMG prototype was evaluated experimentally in order to validate the simulated results. The test setup is shown in Figure 10, which consists of a prototype FMMG attached by a pulley to a brushless DC Servo motor. The motor allows for precise control of the shaft speed to ensure that accurate measurements are taken. A Lorenz DR-3000 torque sensor is placed on the shaft between the motor and gear pulley to take measurements as the reference angle of a single rotor varies. Couplings are placed on either side of the torque sensor to protect it and

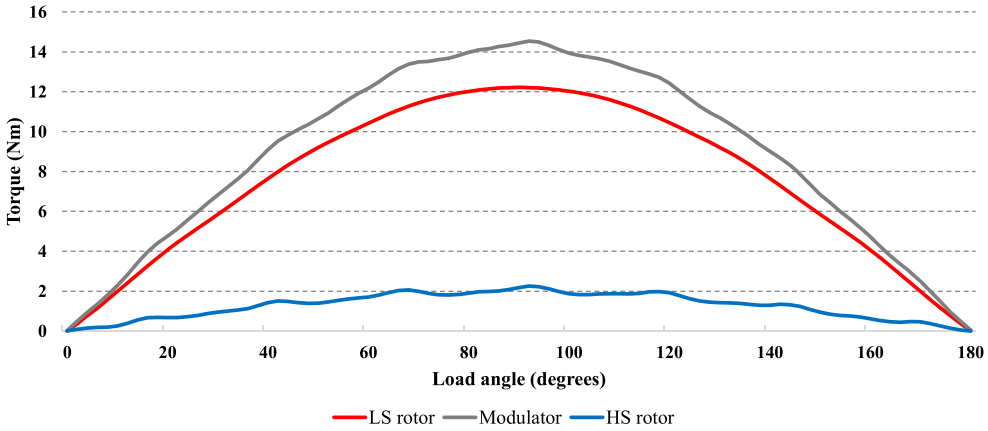

Figure 9. 2-D FEM calculated torque-load angle curves of an axial flux FMMG.

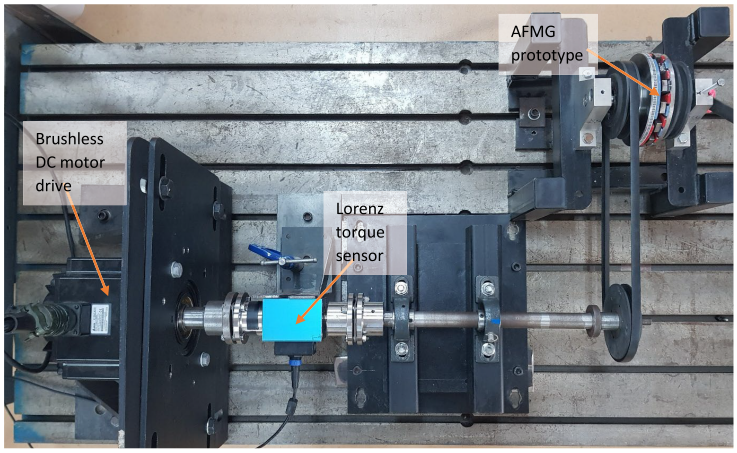

Figure 10. Experimental test set-up for the load angle measurements of an axial flux FMMG.

ensure that it is not damaged due to any overload of forces. The shaft is supported by a stand on the opposite side of the motor to keep it stationary, and the torque sensor and motor are connected via USB 2.0 cables to a laptop to record the measurements during testing.

Since the torque on the LS rotor has a smooth profile, it was decided to perform the static torque-load angle test on LS rotor. Figure 11 shows a close-up of the axial flux FMMG prototype at the initial position. It can be seen that the three disc offset angles, θ_H, θ_M, and θ_L, are fully aligned, which means the load angle $\delta_g = 0$. For this test, the HS rotor disc was held stationary with a G-clamp while the LS rotor disc was turned by the servo motor at 0.5 rev/min. The sampling rate of the torque sensor was set as 25 samples/sec. Figure 12 shows the measured torque as a function of load angles together with the predicted results, which confirms that the maximum torque of the FMMG occurs at a load angle of 90°. For this specific FMMG prototype, the corresponding mechanical displacement angle is $90°/p_L = 7.5°$, which is exactly a half PM pole-pitch angle.

So far, the experimental investigations have been limited to the condition where only one FMMG component rotates while keeping the other two stationary. To demonstrate the load angle of FMMGs under steady-state conditions, further tests are performed where the FMMG operates under different load conditions.

For the setup shown in Figure 13(a), two pulley couplings were attached to each FMMG rotor disc. The LS rotor disc is connected to the brushless DC servo motor and driven at a constant speed of 30 rev/min. The HS rotor disc is connected to a PM Vernier machine, which operates in generator mode feeding an adjustable RLC load and acts as the load to the FMMG. With the gear ratio of 1 : 6,

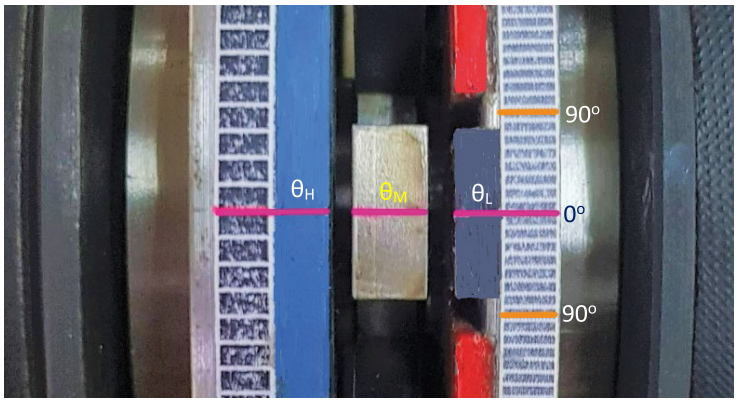

Figure 11. A close-up picture of the axial flux FMMG prototype showing the offset angles of each disc at no-load condition.

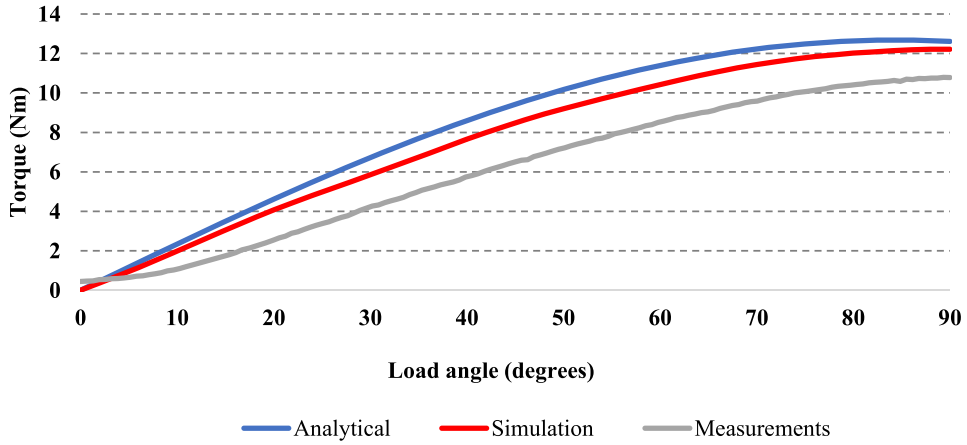

Figure 12. Comparison of the measured and predicted torque-load angle characteristics.

the HS rotor disc rotates at 180 rev/min in the opposite direction.

Since the modulator of the FMMG is stationary, the centre line of the top surface on one of the modulator pole-pieces is used as the reference, which means $\theta_M = 0°$ and leaves us with two more degrees of rotational freedom, i.e., rotation of the LS and HS rotor discs. Considering the point in time at which one of the LS magnet poles aligns with the centre line of the marked stationary modulator pole-piece, the angle θ_L is thus taken as 0. At this point, the angular position on the HS rotor disc, θ_H, can be easily observed and converted to the load angle using $\delta_g = p_H\theta_H$. Using a strobe-light, the exact points in time for different load torques are captured by a camera as shown in Figures 13(b)–13(e). It is shown that each load condition is associated with a specific load angle of an FMMG under steady-state operation. With an increase in load torque, the load angle also increases.

5. THE USE OF LOAD ANGLE IN FMMG AND MGM DESIGN

With the concept of load angle, better understanding of angular relationship among three FMMG components can be developed. The finite element modelling of an FMMG can also be made simpler by selecting appropriate initial angles. Since magneto-static FE solution is usually used to model an FMMG, a common practice is to position the gear components so that the peak torque can be realized [23], which means $\delta_g = 90°$. An easy way to realize this is to align the PM pole axis of a rotor disc with that of a modulator pole-piece and then position the PM pole axis of the other rotor disc with an offset mechanical angle of $90°/p_{L,H}$ as illustrated in Figure 8.

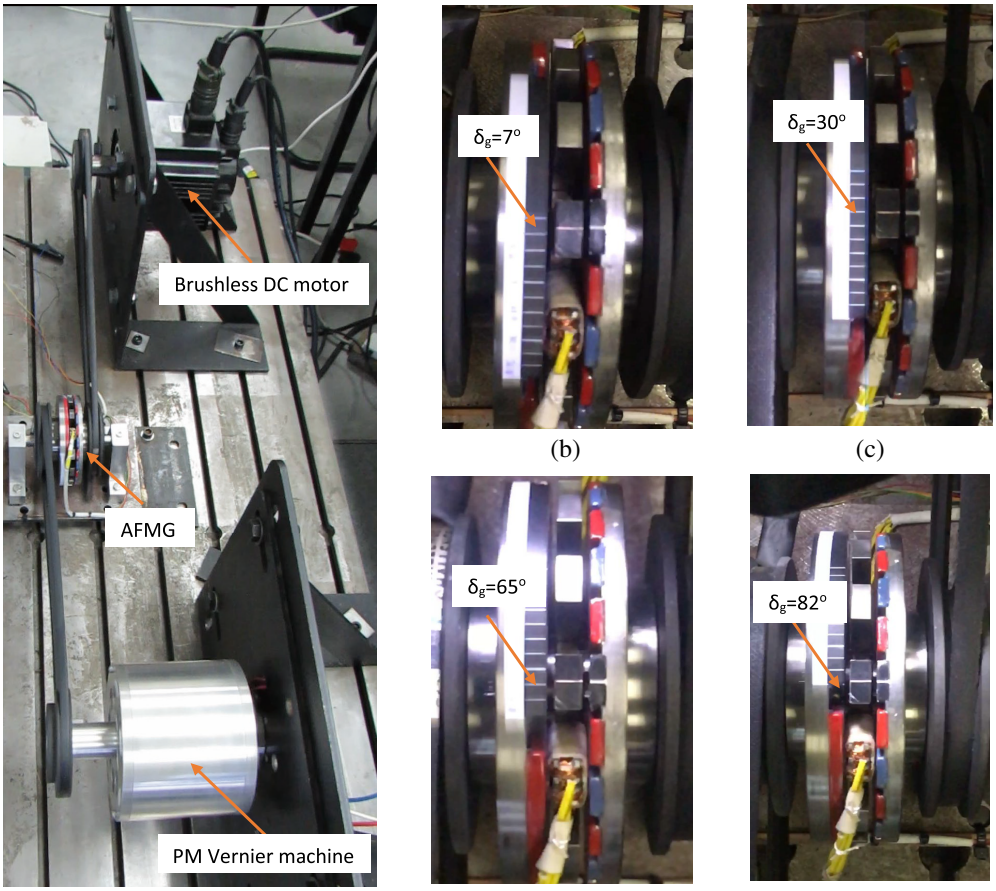

Figure 13. Load angle tests of the axial flux FMMG prototype under steady-state conditions, where (a) test set-up, (b)–(e) steady-state operation under different loads showing respective load angles.

It should be noted that if the losses of an FMMG can be ignored, the load angles measured from steady-state or static condition under the same load torque should be identical. However, owing to the core losses, the load angle of an FMMG under steady-state is always greater. This offers an alternative way of determining rotation losses of an FMMG by observing the difference between estimated load angle δ_g^* and true load angle δ_g. The torque associated with these two load angles can be obtained by either FE calculation or measurements, which are then used to determine the rotational loss (core, frictional and windage losses) of an FMMG.

In classical electrical machine theory, the load angle parameter of a synchronous machine closely relates to its power transfer capability and stability. It is of critical importance to monitor and control the load angle of the machine to safeguard its reliable operations. Likewise, from an operational perspective, it is desirable to operate an FMMG within its maximum torque capability, i.e., its load angle $\delta_g < 90°$. Otherwise, the FMMG will move into a unstable region causing pole-slipping and eventual disengagement between input and output ports. A reengaging of the FMMG usually requires a complete stop of the system. Thus, it is important to monitor the load condition of an FMMG to ensure a smooth operation of the system, especially for certain safety critical applications. The load angle parameter could be very useful for the condition monitoring of FMMGs.

For magnetically geared electrical machines where an FMMG and a PM machine are integrated into a single volume, it is important to ensure a balanced design between the gear and machine parts. A method has been proposed in [21] to characterize a magnetically geared machine (MGM) using a single FE solution under a specific load angle. This could greatly simplify the design optimization process of these complicated MGMs.

6. CONCLUSION

In this paper, a detailed derivation of the load angle of flux modulated magnetic gears is presented, which is validated by both FE simulation and experimental measurements. The study shows that an FMMG does not transfer any torque at its minimum load angle ($\delta_g = 0°$) and attains its maximum torque capacity at a load angle of 90°. This implies that the load angle parameter of an FMMG has a similar significance to that of a classical synchronous machine. By utilizing the load angle concept, the torque characteristics of an FMMG can be expressed as a function of load angle alone, regardless of the number of PM poles or physical angles. This simplifies the modelling process and allows for more convenient comparison of different FMMGs under specific load conditions. Furthermore, the paper also explores the potential significance and applications of the load angle concept.

To facilitate experimental measurements and observations, an axial flux FMMG was selected in this research. However, it is worth noting that the load angle concept and angular relationship derived from the study are also applicable to other FMMG topologies.

To make it viable for some practical applications, a simpler way of determining the load angle of an FMMG is clearly needed. The main challenge is the acquisition of angular positions of FMMG rotors, which calls for more innovative methods or magnetic sensing techniques. Future studies should be encouraged to address these challenges.

ACKNOWLEDGMENT

The authors would like to thank Daniël Loubser, Kansiime Jasper, Andre Swart and Pietro Petzer for their contribution towards the realization and testing of the prototype.

APPENDIX A. LIST OF SYMBOLS

Symbols	Definition	Symbols	Definition
δ_g	Load angle	G_M	Gear ratio
θ_L	LS rotor position	θ_H	HS rotor position
p_H	PM pole-pairs on HS rotor	p_L	PM pole-pairs on LS rotor
ω_H	Angular velocity of HS rotor	ω_L	Angular velocity of LS rotor
ω_M	Angular velocity of modulator	q_M	Number of modulator segments
Z_H	HS air-gap width	Z_L	LS air-gap width
h_x	General component thickness	p_x	General amount of pole-pairs on rotor
$\mathcal{F}_H$	MMF of HS rotor	M_H	MMF harmonic magnitude of HS PM
$\mathcal{F}_L$	MMF of LS rotor	M_L	MMF harmonic magnitude of LS PM
ϕ_{TL}	Total flux in LS air-gap	$\mathcal{P}_{Mod}$	Reluctance due to modulator segments
ϕ_H	Flux in HS air-gap	ϕ_{Hm}	Modulated flux in LS air-gap
ϕ_L	Flux in LS air-gap	ϕ_{Lm}	Modulated flux in HS air-gap
ϕ_{Tx}	General total flux in a air-gap	$\mathcal{P}$	Permeance function of axial-flux path
ϕ_{TH}	Total flux in HS air-gap	$\mathcal{P}_{avg}$	Reluctance of yokes, air-gaps & PMs
$B(r,\theta)$	Flux density in region	$\omega_{j,k}$	Angular speed relations for HS rotor
A_x	Air-gap effective surface area	$\omega_{i,k}$	Angular speed relations for LS rotor
W'_{HS}	Co-energy in HS air-gap	$I_{\phi_{THS}}$	Integral of total flux in HS air-gap
W'_{LS}	Co-energy in LS air-gap	$I_{\phi_{TLS}}$	Integral of total flux in LS air-gap
r_i	Inner region radius	$p_{j,k}$	Pole-pair relationship for HS rotor
r_o	Outer region radius	$p_{i,k}$	Pole-pair relationship for LS rotor
T_{HS}	Torque on HS rotor	ϕ_x	General flux in adjacent airgap
T_{LS}	Torque on LS rotor	ϕ_{xm}	General modulated flux in opposite airgap
T_M	Torque on modulator	$\lvert T_x(\delta_g)\rvert$	Torque at variable load angle

APPENDIX B. INTEGRATION OF FLUX EQUATIONS

The following derivations is used for the integration of modulated harmonics [22]:

$$\phi_x = \int_0^{2\pi} \cos(ax+b)\cos(cx+d)dx \tag{A1}$$

Using the identity

$$\cos(a \pm b) = \cos(a)\cos(b) \mp \sin(a)\sin(b) \tag{A2}$$

the integrand of the flux can be expanded

$$\begin{aligned} \cos(ax+b)\cdot\cos(cx+d) &= (\cos ax\cdot\cos b - \sin ax\cdot\sin b)\cdot(\cos cx\cdot\cos d - \sin cx\cdot\sin d) \\ &= \cos b\cdot\cos d\cdot\cos ax\cdot\cos cx - \cos b\cdot\sin d\cdot\cos ax\cdot\sin cx \\ &\quad - \sin b\cdot\cos d\cdot\sin ax\cdot\cos cx + \sin b\cdot\sin d\cdot\sin ax\cdot\sin cx \end{aligned} \tag{A3}$$

Substituting into (A2) the integral expands to

$$\begin{aligned} \phi_x &= \cos b\cdot\cos d\int_0^{2\pi}\cos ax\cdot\cos cxdx - \cos b\cdot\sin d\int_0^{2\pi}\cos ax\cdot\sin cxdx \\ &\quad - \sin b\cdot\cos d\int_0^{2\pi}\sin ax\cdot\sin cxdx - \sin b\cdot\sin d\int_0^{2\pi}\sin ax\cdot\sin cxdx \end{aligned} \tag{A4}$$

If $a = c$ the result is

$$\phi_x = \pi\cdot(\cos b\cdot\cos d + \sin b\cdot\sin d) = \pi\cdot\cos(b-d) \tag{A5}$$

If $a = -c$ the result is

$$\phi_x = \pi\cdot(\cos b\cdot\cos d - \sin b\cdot\sin d) = \pi\cdot\cos(b+d) \tag{A6}$$

For the case where $|a| \neq |c|$ the equation is reduced to zero.

The integral of the flux equations can be therefore described as

$$\phi_x = \begin{cases} \pi\cdot\cos(b-d) & \text{if } a = c \\ \pi\cdot\cos(b+d) & \text{if } a = -c \\ 0 & \text{otherwise} \end{cases} \tag{A7}$$

if $a = c$ and $b = d$ the integration is reduced to

$$\int_0^{2\pi}\cos^2(ax+b)dx = \pi \tag{A8}$$

REFERENCES

1. Tlali, P. M., R.-J. Wang, and S. Gerber, "Magnetic gear technologies: A review," *2014 International Conference on Electrical Machines (ICEM)*, 544–550, Berlin, 2014.
2. Li, K. and J. Z. Bird, "A review of the volumetric torque density of rotary magnetic gear designs," *2018 XIII International Conference on Electrical Machines (ICEM)*, 2016–2022, Alexandroupoli, 2018.
3. McGilton, B., R. Crozier, A. McDonald, and M. Mueller, "Review of magnetic gear technologies and their applications in marine energy," *IET Renewable Power Generation*, Vol. 12, No. 2, 174–181, 2018.
4. Wang, Y., M. Filippini, N. Bianchi, and P. Alotto, "A review on magnetic gears: Topologies, computational models, and design aspects," *IEEE Transactions on Industry Applications*, Vol. 55, No. 5, 4557–4566, Sept.–Oct. 2019.
5. Ruiz-Ponce, G., M. A. Arjona, C. Hernandez, and R. Escarela-Perez, "Review of magnetic gear technologies used in mechanical power transmission," *Energies*, Vol. 16, No. 4, 1721, 2023.
6. Rens, J., K. Atallah, S. D. Calverley, and D. Howe, "A novel magnetic harmonic gear," *2007 IEEE International Electric Machines & Drives Conference*, 698–703, Antalya, Turkey, 2007.

7. Huang, C. C., M. C. Tsai, D. G. Dorrell, and B. J. Lin, "Development of a magnetic planetary gearbox," *IEEE Transactions on Magnetics*, Vol. 44, No. 3, 403–412, Mar. 2008.
8. Wang, R.-J., A. Matthee, S. Gerber, and P. M. Tlali, "Calculation of torque performance of a novel magnetic planetary gear," *IEEE Magnetics Letters*, Vol. 7, 1–5, Art no. 1303805, 2016.
9. Atallah, K. and D. Howe, "A novel high-performance magnetic gear," *IEEE Transactions on Magnetics*, Vol. 37, No. 4, 2844–2846, Jul. 2001.
10. Johnson, M., M. C. Gardner, H. A. Toliyat, S. Englebretson, W. Ouyang, and C. Tschida, "Design, construction, and analysis of a large-scale inner stator radial flux magnetically geared generator for wave energy conversion," *IEEE Transactions on Industry Applications*, Vol. 54, No. 4, 3305–3314, Jul.–Aug. 2018.
11. Li, K., S. Modaresahmadi, W. B. Williams, J. D. Wright, D. Som, and J. Z. Bird, "Designing and experimentally testing a magnetic gearbox for a wind turbine demonstrator," *IEEE Transactions on Industry Applications*, Vol. 55, No. 4, 3522–3533, Jul.–Aug. 2019.
12. Kowol, M., J. Kołodziej, M. Jagieła, and M. Łukaniszyn, "Impact of modulator designs and materials on efficiency and losses in radial passive magnetic gear," *IEEE Transactions on Energy Conversion*, Vol. 34, No. 1, 147–154, Mar. 2019.
13. Lee, J., et al., "Design and analysis of the coaxial magnetic gear considering the electromagnetic performance and mechanical stress," *IEEE Transactions on Applied Superconductivity*, Vol. 30, No. 4, 1–5, Jun. 2020.
14. Uppalapati, K. K., M. D. Calvin, J. D. Wright, J. Pitchard, W. B. Williams, and J. Z. Bird, "A magnetic gearbox with an active region torque density of 239 N·m/L," *IEEE Transactions on Industry Applications*, Vol. 54, No. 2, 1331–1338, Mar.–Apr. 2018.
15. Gardner, M. C., B. E. Jack, M. Johnson, and H. A. Toliyat, "Comparison of surface mounted permanent magnet coaxial radial flux magnetic gears independently optimized for volume, cost, and mass," *IEEE Transactions on Industry Applications*, Vol. 54, No. 3, 2237–2245, May–Jun. 2018.
16. Chen, Y., W. N. Fu, S. L. Ho, and H. Liu, "A quantitative comparison analysis of radial-flux, transverse-flux, and axial-flux magnetic gears," *IEEE Transactions on Magnetics*, Vol. 50, No. 11, 1–4, Nov. 2014.
17. Johnson, M., A. Shapoury, P. Boghrat, M. Post, and H. A. Toliyat, "Analysis and development of an axial flux magnetic gear," *IEEE Energy Conversion Congress and Exposition (ECCE)*, 5893–5900, 2015.
18. Misron, N., L. Mohd Saini, I. Aris, C. A. Vaithilingam, and H. Tsuyoshi, "Simplified design of magnetic gear by considering the maximum transmission torque line," *Applied Sciences*, Vol. 10, No. 23, 8581, 2020.
19. Filippini, M. and P. Alotto, "Coaxial magnetic gear design and optimization," *IEEE Transactions on Industrial Electronics*, Vol. 64, No. 12, 9934–9942, Dec. 2017.
20. "Magnetic gear: 2D FEM simulation with EMWorks2D inside SOLIDWORKS," available online: https://www.emworks.com/application/magnetic-gear-2d-fem-simulation-with-emworks2d-inside-solidworks (accessed on 20 Feb. 2023).
21. Gerber, S. and R.-J. Wang, "Design and evaluation of a magnetically geared PM machine," *IEEE Transactions on Magnetics*, Vol. 51, No. 8, 1–10, Aug. 2015.
22. Gerber, S., "Evaluation and design aspects of magnetic gears and magnetically geared electrical machines," Ph.D. dissertation, Stellenbosch University, Dec. 2015.
23. Matthee, A., R.-J. Wang, C. J. Agenbach, D. N. J. Els, and M. J. Kamper, "Evaluation of a magnetic gear for air-cooled condenser applications," *IET Electric Power Applications*, Vol. 12, No. 5, 677–683, 2018.